Polydopamine Coated CeO$_2$ as Radical Scavenger Filler for Aquivion Membranes with High Proton Conductivity

Roberto D'Amato [1,†], Anna Donnadio [2,3,*], Chiara Battocchio [4], Paola Sassi [1], Monica Pica [2,3], Alessandra Carbone [5], Irene Gatto [5] and Mario Casciola [1,3]

1   Department of Chemistry, Biology and Biotechnologies, University of Perugia, via Elce di Sotto 8, 06123 Perugia, Italy; roberto.damato@inl.int (R.D.); paola.sassi@unipg.it (P.S.); mario.casciola@unipg.it (M.C.)
2   Department of Pharmaceutical Sciences, University of Perugia, via del Liceo 1, 06123 Perugia, Italy; monica.pica@unipg.it
3   CEMIN, Materiali Innovativi Nanostrutturali per Applicazioni Chimica Fisiche e Biomediche, University of Perugia, via Elce di Sotto 8, 06123 Perugia, Italy
4   Department of Sciences, University of Roma Tre, via della Vasca Navale 79, 00146 Rome, Italy; chiara.battocchio@uniroma3.it
5   CNR ITAE, via S. Lucia Sopra Contesse, 5, 98126 Messina, Italy; alessandra.carbone@itae.cnr.it (A.C.); irene.gatto@itae.cnr.it (I.G.)
*   Correspondence: anna.donnadio@unipg.it
†   Present address: International Iberian Nanotechnology Laboratory, 4715-330 Braga, Portugal.

Abstract: CeO$_2$ nanoparticles were coated with polydopamine (PDA) by dopamine polymerization in water dispersions of CeO$_2$ and characterized by Infrared and Near Edge X-ray Absorption Fine Structure spectroscopy, Transmission Electron Microscopy, Thermogravimetric analysis and X-ray diffraction. The resulting materials (PDAx@CeO$_2$, with x = PDA wt% = 10, 25, 50) were employed as fillers of composite proton exchange membranes with Aquivion 830 as ionomer, to reduce the ionomer chemical degradation due to hydroxyl and hydroperoxyl radicals. Membranes, loaded with 3 and 5 wt% PDAx@CeO$_2$, were prepared by solution casting and characterized by conductivity measurements at 80 and 110 °C, with relative humidity ranging from 50 to 90%, by accelerated ex situ degradation tests with the Fenton reagent, as well as by in situ open circuit voltage stress tests. In comparison with bare CeO$_2$, the PDA coated filler mitigates the conductivity drop occurring at increasing CeO$_2$ loading especially at 110 °C and 50% relative humidity but does not alter the radical scavenger efficiency of bare CeO$_2$ for loadings up to 4 wt%. Fluoride emission rate data arising from the composite membrane degradation are in agreement with the corresponding changes in membrane mass and conductivity.

Keywords: cerium oxide; polydopamine; radical scavenger; proton conductivity; chemical degradation

1. Introduction

In recent years, the need to arrest the effects of climate change is pushing governments worldwide to plan and coordinate efforts to achieve a dramatic reduction in CO$_2$ emissions. This requires a revolution in energy supply toward much more flexible renewable energy systems. Hydrogen offers several benefits for simultaneously decarbonizing transport, housing and industrial sectors. Among hydrogen-based technologies, proton exchange membrane (PEM) fuel cells have revealed promising for stationary and automotive applications. Because of the lifetime targets for large-scale stationary applications ($\approx$40,000 h), as well as for automotive applications (>6000 h) [1], the proton exchange membrane durability represents a key element for the longevity of the device. However, several factors limit the membrane's long-term stability. A source of membrane degradation is due to chemical degradation caused by radical species such as H$^\bullet$, OH$^\bullet$ and HOO$^\bullet$ [2–6], which gives rise to a thinning of the membrane leading to short the lifetime of PEM fuel cells. A strategy to mitigate such radical attacks consists of the incorporation of radical scavengers.

For example, the introduction of metal cations, such as Ce^{4+} and Mn^{2+}, or their oxides, including CeO_2 and MnO_2, revealed to be effective in mitigating the chemical degradation of PFSA (PerFluoroSulfonic Acid) polymers [7–15] because, due to the multivalent oxidation state of the metals, they can act as catalysts for the decomposition of hydroxyl and hydroperoxyl radicals.

In a recent paper, it was reported that CeO_2 nanoparticles dispersed in an Aquivion matrix undergo partial solubilization at relative humidity in the range 50–90%, when the temperature is increased from 80 to 110 °C [16]. As a consequence, for CeO_2 loadings greater than 2 wt%, a decrease in the composite membrane conductivity was observed with increasing temperature, in such a way that the larger the CeO_2 loading, the more severe the conductivity drop. It was also found that the formation of a protective shell on the oxide surface, made of fluorophosphonates bonded to cerium ions through the $–PO_3$ groups, partially avoided the conductivity drop. However, the organically modified CeO_2 nanoparticles show reduced radical scavenger activity in comparison with the pristine nanoparticles. A reasonable compromise between stable conductivity and improved membrane stability towards radical was reached by bonding a fluorobenzyl phosphonate (hereafter Bz) to the CeO_2 surface. Based on these results and taking into account that the phosphonate can be hydrolyzed after long-term operation under conditions of high membrane hydration, it was of interest to coat the oxide surface with a polymeric film that could be hydrolytically more stable than the phosphonate coating.

To this aim, polydopamine (PDA, Scheme 1) was chosen for its strong and universal adhesion ability and the simple deposition process through self-polymerization in an alkaline aqueous solution [17–33].
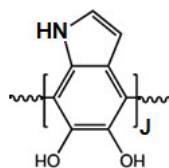
Scheme 1. Structure of polydopamine.

The preparation of PDA-based materials has rapidly advanced in recent years with a significant expansion in their applications [21–34], becoming one of the most attractive areas within the materials field including surface modification, biosensing [35,36], nanomedicine [37] and systems for energy applications [38–43]. In particular, PDA allows obtainment of a beneficial and advantageous interface between CeO_2 and PFSA improving the lifetime of PEM fuel cells [44].

This paper reports the formation of a PDA film on the surface of CeO_2 nanoparticles by dopamine polymerization in a water suspension of CeO_2, and the use of this composite material ($PDA@CeO_2$) as a filler of membranes made of Aquivion.

Membranes containing 3 and 5 wt% filler loadings were characterized by conductivity measurements at 80 and 110 °C, in the RH range 50–90%, to test their stability at increasing temperature. These membranes were also subjected to accelerated ageing by using the Fenton reagent to assess the radical scavenger efficiency of the filler based on the fluoride emission rate (FER). Both conductivity and FER data collected in the present work are compared with the corresponding literature data for composite Aquivion membranes filled with pristine CeO_2 and $Bz@CeO_2$. The most stable membrane was also characterized by Open Circuit Voltage (OCV) stress tests coupled with hydrogen crossover determinations.

2. Materials and Methods

2.1. Materials

Cerium (III) nitrate hexahydrate ($Ce(NO_3)_3 \cdot 6H_2O$) was from Carlo Erba. A 20 wt% Aquivion dispersion in water (D83-6A, ionomer equivalent weight = 830 g/equiv.) was kindly provided by Solvay Specialty Polymers, Italy. The citric acid ($C_6H_8O_7 \cdot H_2O$),

dopamine and all other reagents were purchased from Sigma-Aldrich and used without purification.

2.2. Synthesis of CeO₂ and PDA@CeO₂

Nanopolyhedral CeO_2 was synthesized by sol-gel followed by thermal decomposition according to the procedure reported in 15. Three composite materials made of cerium dioxide nanoparticles coated with PDA were prepared by reacting, under stirring, a weighed amount of cerium dioxide nanoparticles with 10 mL of a dopamine hydrochloride solution: specifically, 100 mg CeO_2 with 0.01 M dopamine (hereafter Sample 1), 150 mg CeO_2 with 0.05 M dopamine (Sample 2) or with 0.1 M dopamine (Sample 3). A suitable amount of NaOH 0.1 M was added to keep pH at 8.5 to achieve a polydopamine film on the nanoparticles. Subsequently, the dispersion was stirred for 24 h at room temperature in dark conditions. The powder was then recovered by centrifugation, washed with water several times and then dried at 80 °C overnight. These composite materials will hereafter be indicated as PDAx@CeO_2, where x is the PDA weight percentage in the composite.

2.3. Membrane Preparation

The Aquivion dispersion in water was cast on a Petri dish and dried at 80 °C in an oven. The resulting membrane was dissolved in propanol (1 g in 20 mL) at 80 °C. A weighted amount of pristine CeO_2 or PDA coated CeO_2 nanoparticles was added to 20 mL of the Aquivion dispersion in propanol. The mixtures were treated with ultrasounds for 10 min, stirred for 2 h, cast by an Elcometer Doctor Blade Film Applicator on a glass support and dried in an oven at 80 °C. After that, all membranes were treated according to the following procedure: 2 h in HCl 1 M, 1 h in H_2O at room temperature, 2 h at 90 °C and 1 h at 160 °C. Composite membranes, 20–25 μm thick, containing 3% and 5% wt% of PDAx@CeO_2 were prepared. The same procedure was used to prepare the neat Aquivion membrane.

2.4. Ex Situ Accelerated Ageing

Accelerated ex situ ageing tests were performed by treating a membrane sample (ca. 60 mg) with 20 mL of the Fenton reagent (20 ppm iron sulfate, $FeSO_4 \cdot 7H_2O$, in 30 wt% hydrogen peroxide solution) for 4 h, at 75 °C. The membrane was then washed with deionized water and dried at room temperature. The concentration of fluoride ions in the Fenton's solution was determined using a Mettler Toledo fluoride ion-selective electrode. The pH was kept in the range of 5–7 using an electrolyte solution (TISAB) with the appropriate total ionic strength adjustment buffer [16].

2.5. Conductivity Measurements

The in-plane conductivity was determined according to the four-point impedance technique on 5 cm $\pm$ 0.5 cm membrane strips at frequencies ranging from 10 Hz to 100 kHz, with 100 mV, signal amplitude using an Autolab, PGSTAT30 potentiostat/galvanostat equipped with a frequency response analyzer module, as described in ref. [45].

2.6. Transmission Electron Microscopy

Transmission electron microscopy (TEM) images were collected on powders previously dispersed in ethanol by using a sonicator and then supported and dried on copper grids (200 mesh) coated with Formvar carbon film. A Philips 208 transmission electron microscope, operating at an accelerating voltage of 100 kV, was used.

2.7. X-ray Diffraction

X-ray diffraction (XRD) patterns of powders were collected with a Philips X'Pert PRO MPD diffractometer as described in [46].

2.8. Ionic Exchange Capacity Determination

Membrane samples (~250 mg) were dried at 120 °C for 3 h, weighed and then equilibrated in 20 mL of 0.1 M NaCl overnight to exchange the membrane protons with Na^+ ions. The solution was titrated, in the presence of the membrane, with 0.01 M NaOH through a Radiometer automatic titrimeter (TIM900 TitraLab, Radiometer Copenhagen, Denmark), according to the equilibrium point method. The reported Ionic Exchange Capacity (IEC) values are the average of five replicate titrations [16].

2.9. ATR-FTIR

IR spectra were collected by means of Bruker Optics Alpha FTIR instrument equipped with a Platinum-ATR accessory (Bruker Optics, Karlsruhe, Germany). The samples were deposited on the diamond ATR (attenuated total reflection) crystal and their spectrum was recorded at room temperature over the range 5000–400 cm^{-1} with a 2 cm^{-1} resolution.

2.10. Near Edge X-ray Absorption Fine Structure (NEXAFS)

NEXAFS spectra were acquired at the ELETTRA storage ring using the BEAR (bending magnet for emission absorption and reflectivity) beamline, installed at the left exit of the 8.1 bending magnet exit. The BEAR beamline has a bending magnet as a source, and beamline optics deliver photons from 5 eV up to 1600 eV; the degree of ellipticity of the beam is selectable. The experimental station is in UHV, and it is equipped with a movable hemispherical electron analyzer and a set of photodiodes to collect angle-resolved photoemission spectra, optical reflectivity and fluorescence yield. In the here reported experiments ammeters to measure drain current from the sample were used. We collected C K-edge and O K-edges spectra at a magic-incidence angle (54.7°) of the linearly polarized photon beam with respect to the sample surface. Both photon energy and spectral resolution were calibrated and experimentally tested using the absorption K-edges of Ar, N_2 and Ne. The acquired spectra were normalized by subtracting a straight line that fits the part of the spectrum below the edge and imposing an Absorption Intensity value of 1 at 320.00 eV for C K-edge and 560.00 eV for O K-edge.

2.11. In Situ Accelerated Stress Tests

Gas diffusion electrodes (GDEs) were prepared by a spray technique. Sigracet 25- BC Gas Diffusion Layer (SGL), was used as a GDL, and the catalytic ink was deposited onto its surface, as reported elsewhere [47]. The same Pt loading of 0.2 mg cm^{-2} was used for cathode and anode. The GDEs were hot-pressed, at a pressure of 20 kgcm^{-2} for 5 min at 125 °C, onto Aquivion membrane to realize the Membrane-Electrode Assemblies (MEAs). The Accelerated stress tests (AST) in a H_2/air 25 cm^2 single cell, at the Open Circuit Voltage and steady-state conditions, were carried out in the following operative conditions: 80 °C, 50% RH, 1.5 bar$_{abs}$, flow rate 1.5 and 2 times the stoichiometry for H_2 and air, respectively [48]. The tests were performed by connecting the single cell with a commercial test station (Fuel Cell Technologies Inc.), and an AUTOLAB Metrohm Potentiostat/Galvanostat with a 20 A current booster to carry out the electrochemical diagnostics measurements. Linear Sweep Voltammetry (LSV) was carried out by feeding the anode and cathode with hydrogen and nitrogen, respectively, to determine the H_2 crossover. A potential scan, ranging from 0 to 0.8 V with a scan rate of 4 mVs^{-1}, was used to perform the LSV.

3. Results and Discussion

3.1. Filler Materials

The composite samples obtained by reacting dopamine with an aqueous dispersion of CeO_2 nanoparticles were first characterized by ATR-FTIR spectroscopy to prove the PDA formation. In Figure 1 the ATR spectrum of Sample 3 (see Section 2.2) is compared with the spectra of CeO_2 and PDA. The main bands of PDA are recognized in the spectrum of the composite. Specifically, the bands centered at 1596 and 1510 cm^{-1} can be attributed to (C=C) and (C–N) stretching modes, respectively, and confirm the presence of

aromatic amine species in the coating. The band at ca. 1600 cm^{-1}, as well as the feature at 1723 cm^{-1}, are assigned to C=O quinone groups. All these peaks increase in intensity as dopamine concentration increases in the reacting mixture, which indicates the increasing PDA concentration in the coatings [49–52].
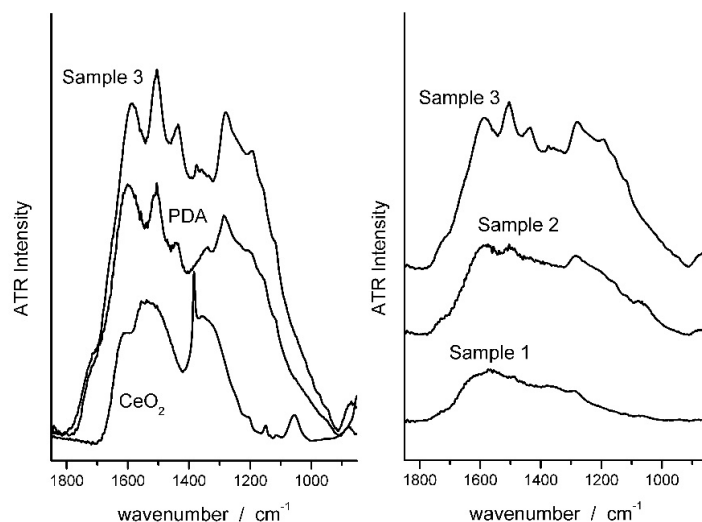

Figure 1. ATR spectra of CeO$_2$, PDA and PDAx@ CeO$_2$ samples.

PDAx@CeO$_2$ materials were further characterized by NEXAFS to get information about the PDA oxidation state. All samples show similar features in C K-edge spectra (Figure 2). The main feature appears in the π* region, at about 286 eV, and is attributed to C1s –π*C=O transitions [53]. A couple of features around 289 eV are indicative of the N–containing ring (C=C π* and C–N σ* excitations), confirming the molecular structure integrity. The large and broad feature at about 300 eV in σ* spectral region is associated with C1s – σ*C=O excitations. C K-edge spectra suggest an abundance of C=O functional groups in the examined samples.
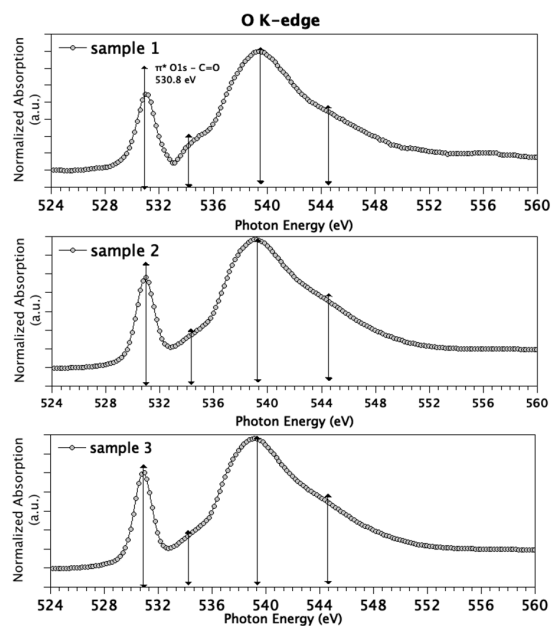
Figure 2. C K-edge spectra measured for Sample 1 (**top**), Sample 2 (**middle**) and Sample 3 (**bottom**).

As with C K-edge spectra, O K-edge spectra (Figure 3) are similar for the three measured samples. The energies of the features in O K-edge spectra and proposed assignments

are summarized as follows: the sharp and intense peak centered at 530.8 eV is attributed to the transition of 1 s electrons of C=O groups to antibonding molecular orbitals π*C=O, while the small feature around 534 eV is indicative for transitions of 1 s electrons of hydroxyl-like O atoms to π*O–C and 3 s/σ*O–H [54]. As for the σ* region, features around 540 and 544 eV are associated with O1s C–O and C=O σ* transitions, respectively.
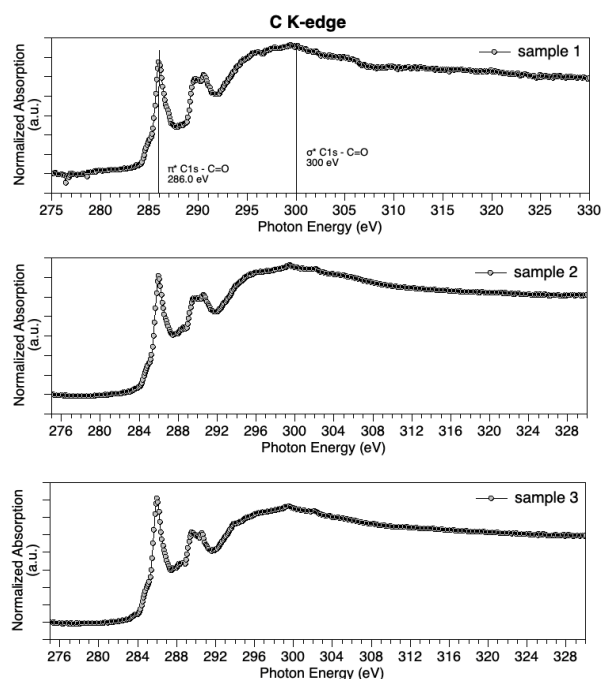
Figure 3. O K-edge spectra measured for Sample 1 (**top**), Sample 2 (**middle**) and Sample 3 (**bottom**).

Since in NEXAFS data analysis the so-called *building block approach* can be successfully applied [55] (i.e., the NEXAFS spectrum of a complex molecule or sample can be built by summing up the contribution arising by the different functional groups, weighted for their abundance in the sample), the presence of strong features diagnostic for carbonyl groups, and only weak contributions arising by hydroxyls, suggests that the polymer is mainly in the oxidized state.

The PDA content in the PDAx@CeO$_2$ composite samples was determined by thermogravimetric analysis. The weight loss curves for Samples 1, 2 and 3, as well as for bare CeO$_2$, are displayed in Figure 4. While CeO$_2$ does not present any appreciable loss, the curves of the composites show a small weight loss up to 100 °C, due to the water loss, and a second loss above 200 °C arising from PDA decomposition, which increases with increasing the dopamine concentration used for the polymerization reaction. Based on the second weight loss, the PDA content in anhydrous PDAx@CeO$_2$ turned out to be 10.2 wt% (Sample 1), 24.7 wt% (Sample 2) and 49.5 wt% (Sample 3); these samples will be hereafter indicated as PDA10@CeO$_2$, PDA25@CeO$_2$ and PDA50@CeO$_2$, respectively.

The morphology of CeO$_2$ and the PDAx@CeO$_2$ composites was investigated by TEM. The pictures of Figure 5 reveal that PDA can coat the cerium oxide surface forming an irregular layer without affecting the shape and the dimension of the pristine CeO$_2$ particles, which in all cases lies around 10 nm. In particular, as the amount of PDA in the composite increases, the thickness of the coating becomes more evident reaching a thickness of some nanometers for the highest PDA content.
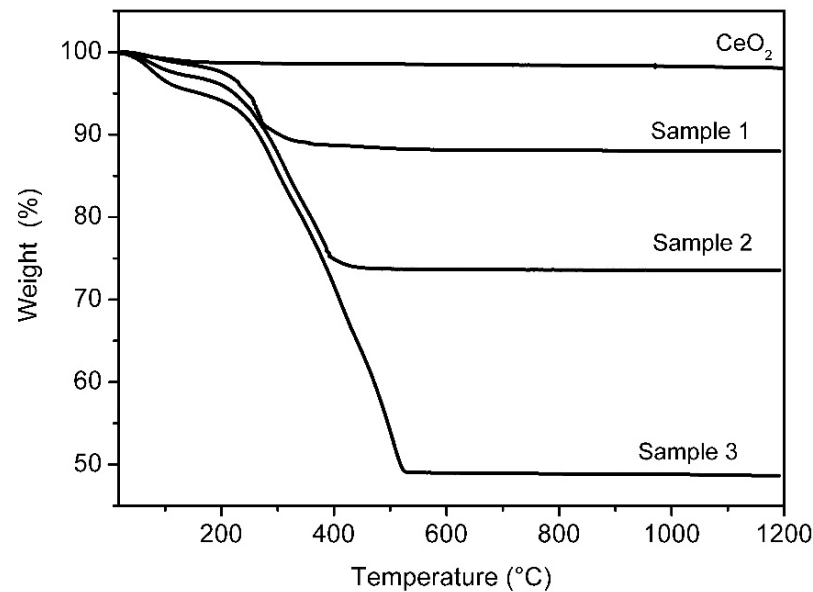
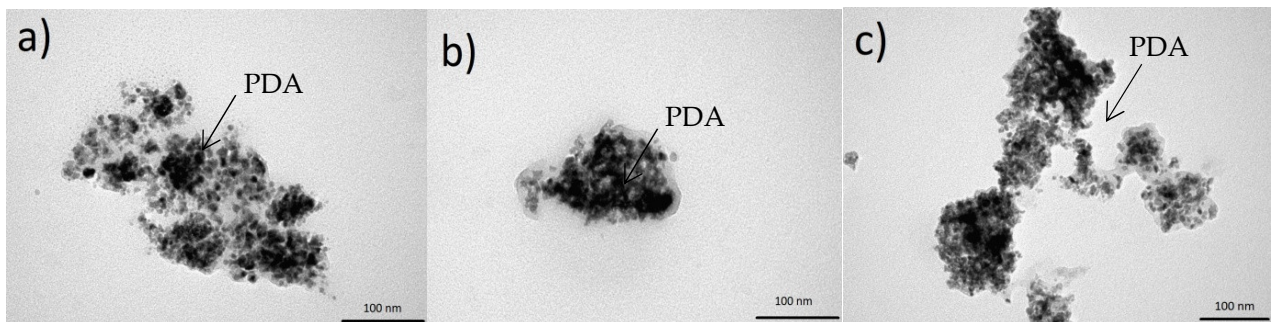**Figure 4.** Weight loss curves for bare CeO_2 and for $PDAx@CeO_2$ samples.

Figure 5. TEM images of (**a**) $PDA10@CeO_2$, (**b**) $PDA25@CeO_2$ and (**c**) $PDA50@CeO_2$.

To use the $PDAx@CeO_2$ materials as fillers of Aquivion composite membranes, we checked that the PDA coating is not soluble in the solvent (propanol) used for membrane preparation. To this aim, 0.05 g of PDA was dispersed in 20 mL of propanol and the mixture was kept under stirring at room temperature for 2 h and then at 80 °C in a closed bottle for 2 h. After centrifugation, the solid was dried at 80 °C. The weight loss curve of the starting material ($PDA13@CeO_2$) is coincident, within the experimental error, with the curve of the treated material ($PDA13@CeO_2$ PrOH 80) thus indicating that PDA is not soluble under the conditions of membrane preparation (data not shown).

X-ray diffraction (XRD) patterns were collected to reveal possible structural modifications or changes in crystallinity induced by the PDA formation. Figure 6 shows that the position and the intensity of the peaks of bare CeO_2 do not change in the PDA coated samples suggesting that the presence of the PDA coating does not affect the CeO_2 crystal structure.

Moreover, in agreement with the TEM images, the particle size calculated using the Scherrer equation lies in the range from 9.9 to 11.2 nm.

The PDA coating of CeO_2 turned out to be insoluble in propanol at 80 °C, which is the solvent for Aquivion 830: this allowed the $PDAx@CeO_2$ materials to be used as fillers of Aquivion based composite membranes.
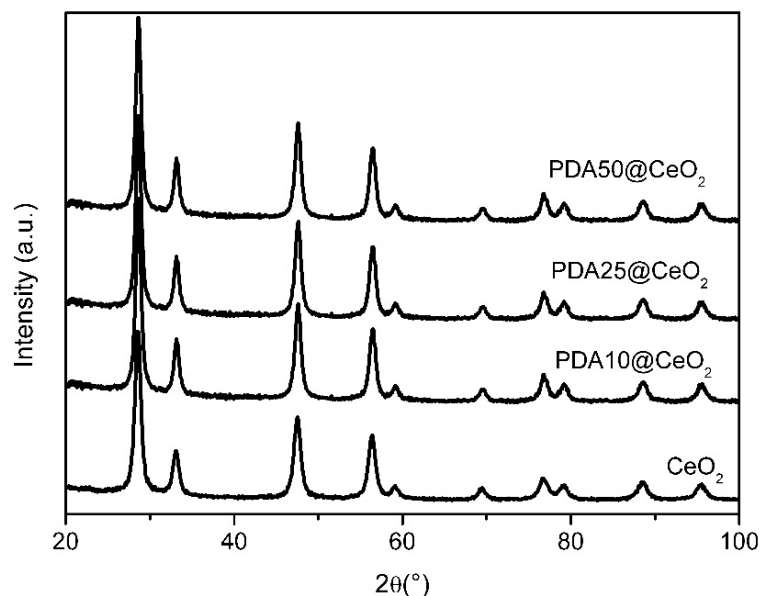
Figure 6. XRD patterns for pristine and coated CeO_2.

3.2. Composite Membranes

The IEC values (in milliequivalents per gram) of the composite membranes with 3 and 5 wt% PDAx@CeO$_2$ loadings (Table 1) are at most by 4% lower than those calculated based on the ionomer weight percentage. In principle, this could be due to the protonation of nitrogen atoms of PDA and/or of surface oxide ions of CeO_2. The fact that, for the same PDAx@CeO$_2$ loading, the IECs show the sequence:

$$IEC(PDA50) > IEC(PDA25) > IEC(PDA10)$$

indicates that the protonation of the oxide ions is mainly responsible for the IEC decrease because the amount of cerium oxide in the filler is minimum for PDA50 and maximum for PDA10.

Table 1. IEC values (meq g^{-1}) of PDAx@CeO$_2$ composite membranes. The IEC values calculated based on the Aquivion wt% (AQ$_{calc}$) are also reported.

wt%	PDA10	PDA25	PDA50	AQ$_{calc}$
3	1.13	1.15	1.16	1.16
5	1.10	1.12	1.15	1.14

Standard deviation = 0.0032.

The conductivity (σ) of membranes containing 3 and 5 wt% PDAx@CeO$_2$ (with x = 10, 25 or 50), as well as the conductivity of a membrane containing 6 wt% PDA10@CeO$_2$, was determined for RH increasing in the range 50–90%, first at 80 °C and then at 110 °C. In all cases, the plot of logσ as a function of RH is linear. As an example, Figure 7 displays the conductivity of composite membranes containing 5 wt% filler together with that of bare Aquivion. At both temperature and for each RH value, the following conductivity sequence is observed:

$$σ(PDA50) > σ(PDA25) > σ(PDA10)$$

which indicates that the conductivity increases with decreasing the CeO_2 content in the filler. Moreover, going from 80 to 110 °C, the conductivity evolution depends also on the CeO_2 mass fraction in the filler in such a way that it increases in the presence of PDA50@CeO$_2$ but keeps nearly constant in the presence of PDA10@CeO$_2$.
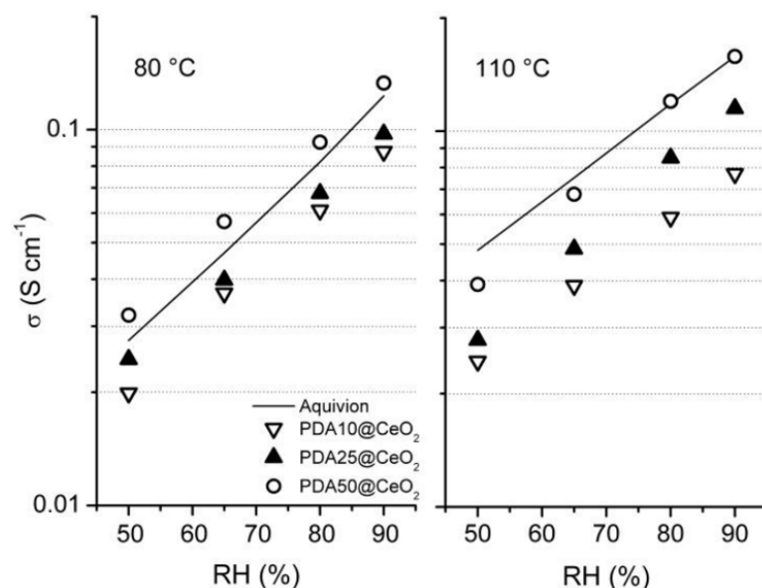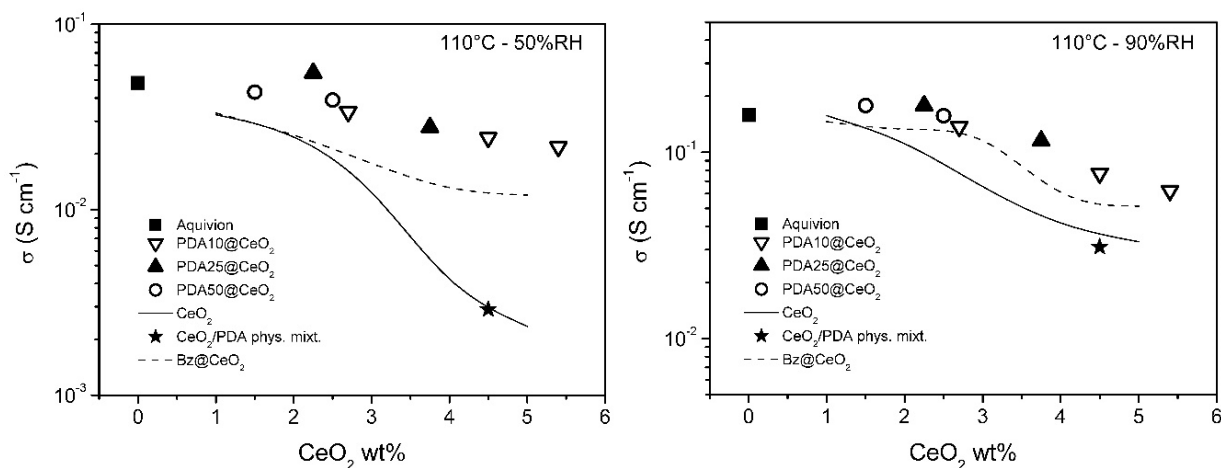
Figure 7. Conductivity as a function of relative humidity, at 80 and 110 °C, for composite Aquivion membranes containing 5 wt% PDAx@CeO$_2$. The conductivity of bare Aquivion is also reported.

A similar trend was already reported for Aquivion/CeO$_2$ composite membranes in a recent work [16] where it was shown that the increase in temperature favors the acid-base reaction between cerium oxide and ionomer protons thus causing an IEC decrease which, depending on CeO$_2$ content, offsets the expected increase in conductivity.

To get insight into the dependence of the conductivity on CeO$_2$ loading, the conductivity of the PDAx@CeO$_2$ composite membranes is plotted in Figures 8 and 9 as a function of CeO$_2$ wt% in the membrane at constant temperature (80 and 110 °C) and RH (50 and 90%). For comparison, the conductivity of composite Aquivion membranes filled with bare CeO$_2$ and Bz@CeO$_2$ is also reported [16]. At 80 °C, the conductivity of the composite membranes filled with PDAx@CeO$_2$ is weakly dependent on CeO$_2$ loading and is close to the conductivity of Aquivion. On the other hand, at 110 °C, the composite membranes become progressively less conductive with increasing of the CeO$_2$ loading so that the membrane with 5.4 wt% CeO$_2$ is by a factor of about 2.5 less conductive than Aquivion both at 50 and 90% RH.
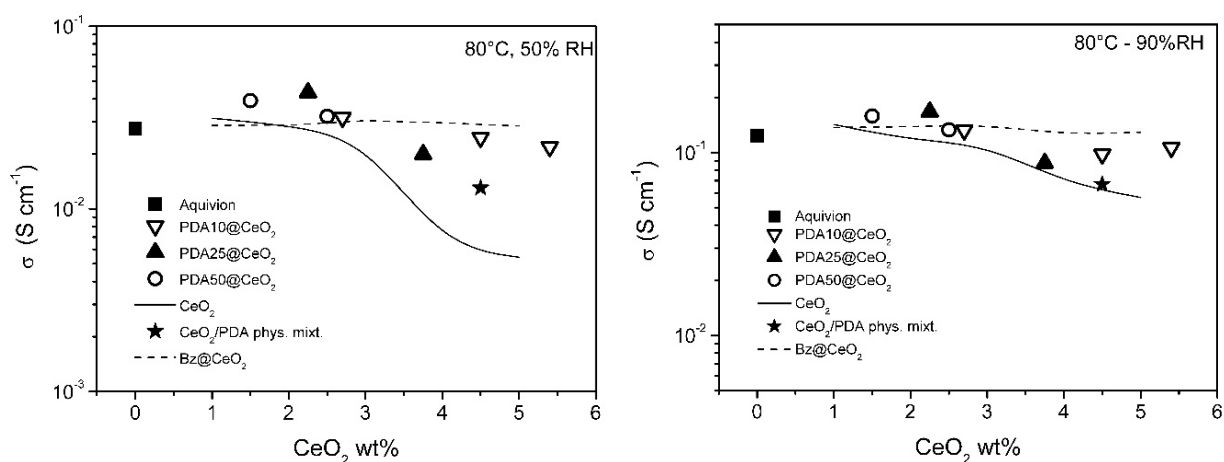
Figure 8. Conductivity as a function of CeO$_2$ loading, at 80 °C, for composite Aquivion membranes filled with PDAx@CeO$_2$ (x = 10, 25 and 50), as well as with the physical mixture PDA/CeO$_2$ (see text). The conductivity of composite Aquivion membranes containing bare CeO$_2$ and Bz@CeO$_2$ (redrawn from ref. [16]) is reported for comparison.

Figure 9. Conductivity as a function of CeO_2 loading, at 110 °C, for composite Aquivion membranes filled with $PDAx@CeO_2$ (x = 10, 25 and 50), as well as with the physical mixture PDA/CeO_2 (see text). The conductivity of composite Aquivion membranes containing bare CeO_2 and $Bz@CeO_2$ (redrawn from ref. [16]) is reported for comparison.

The CeO_2 loading being the same, the conductivity of the $PDAx@CeO_2$ membranes is similar to the conductivity of the $Bz@CeO_2$ membranes except for 110 °C and 50% RH, where the $PDAx@CeO_2$ membranes are more conductive by a factor of ~2 at the highest CeO_2 loadings.

Moreover, the $PDAx@CeO_2$ membranes are always more conductive than the corresponding membranes filled with bare CeO_2 and the difference in conductivity increases with decreasing RH and with increasing filler loading and temperature. As a consequence, at 110 °C and 50% RH, the conductivity of the membrane with $PDA10@CeO_2$ containing 4.5 wt% CeO_2 is by one order of magnitude higher than that of the corresponding membrane containing bare CeO_2.

It was of interest to prove that the better conductivity of the $PDAx@CeO_2$ membranes, in comparison with the corresponding membranes loaded with bare CeO_2, is indeed due to the presence of the PDA shell on the CeO_2 surface. To this end, a composite Aquivion membrane containing the same amount of PDA and CeO_2 as the membrane loaded with 5 wt% $PDA10@CeO_2$ (i.e., 0.5 wt% PDA and 4.5 wt% CeO_2) was prepared by mixing the Aquivion dispersion with a physical mixture of PDA and bare CeO_2. The conductivity of this membrane, determined at 50 and 90% RH, first at 80 °C and then at 110 °C (the asterisk in Figures 8 and 9), was always lower than the conductivity of the membrane loaded with 5 wt% $PDA10@CeO_2$, being in three cases even coincident with the conductivity of the membrane containing 4.5 wt% bare CeO_2. These results show that it is the PDA coating that efficiently protects the cerium oxide particles against the acidic sulfonic groups of the ionomer, thus avoiding to a large extent the severe conductivity drop occurring with bare CeO_2.

To evaluate the membrane resistance towards radical species generated by the decomposition of hydrogen peroxide, ex situ degradation tests were performed by treating the composite membranes with the Fenton solution (see Experimental section). The results of these tests are expressed in terms of fluoride emission rate, FER, defined as the ratio between the mass of released fluoride ions and the initial mass of the anhydrous membranes. Figure 10 shows the FER values of the $PDAx@CeO_2$ composite membranes as a function of CeO_2 loading and, for comparison, the FER values of composite Aquivion membranes filled with bare CeO_2 and $Bz@CeO_2$. The FER values obtained with $PDAx@CeO_2$ are significantly lower than those of $Bz@CeO_2$. Like Bz, the PDA coating prevents to a large extent the decrease in conductivity, but, unlike Bz, it does not compromise the radical scavenger activity of CeO_2. The radical scavenger efficiency of $PDAx@CeO_2$ is nearly coincident with that of membranes loaded with bare CeO_2, for CeO_2 percentage up to 4 wt%, and similar to that for higher loadings: a FER value of 10^{-3} is indeed obtained with

5.4 wt% of PDA coated CeO_2 and with 4.7 wt% of bare CeO_2. It can also be observed that the membranes loaded with 5 wt% PDA50@CeO_2 and with 3 wt% PDA10@CeO_2 have the same FER and close CeO_2 content (2.5 and 2.7 wt%, respectively) but very different PDA content (2.5 and 0.3 wt%, respectively). Thus, the radical scavenger properties of PDAx@CeO_2 are mainly dependent on the CeO_2 weight percentage, while the PDA coating does not shield significantly the radical scavenger activity of CeO_2.
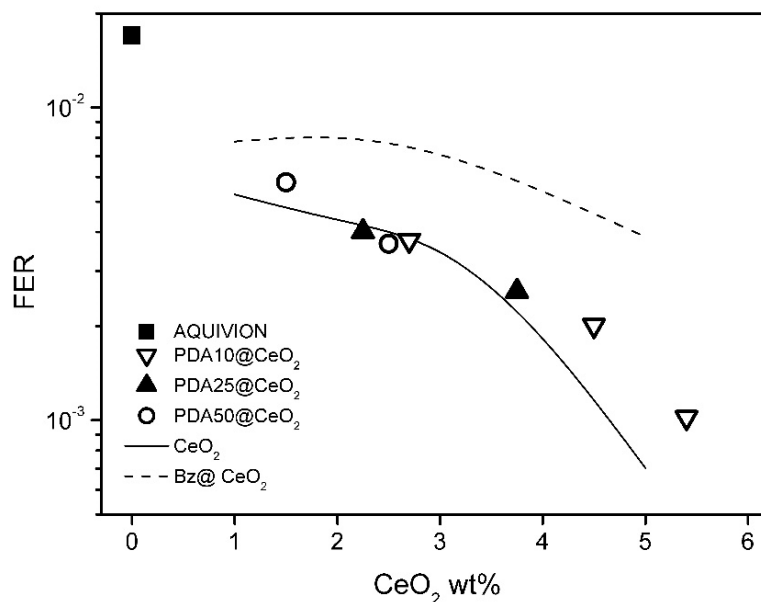
Figure 10. Fluoride emission rate (FER) as a function of CeO_2 content for composite Aquivion membranes filled with PDA10@CeO_2, PDA25@CeO_2 and PDA50@CeO_2. The FER of composite Aquivion membranes containing bare CeO_2 and Bz@CeO_2 (redrawn from ref. [16]) is reported for comparison.

After the Fenton test, the membranes with 3 wt% PDAx@CeO_2 and the membrane with 6 wt% PDA10@CeO_2 were washed with 1 M HCl and water, dried at 120 °C and weighed. The percentage weight loss concerning the initial weight of the anhydrous membrane (Table 2) decreases with increasing the CeO_2 loading in the composite membrane, going from 25.4% for the membrane with 3 wt% PDA50@CeO_2 to 5.9% for the membrane with 6 wt% PDA10@CeO_2.

Table 2. Dry weight and conductivity percentage changes (%Δw and %$\Delta\sigma$) for bare Aquivion and Aquivion composite membranes loaded with PDAx@CeO_2 after the Fenton test.

Filler	Filler wt%	CeO_2 wt%	%Δw	%$\Delta\sigma$
Aquivion	0	0	−22	−25
PDA50@CeO_2	3	1.5	−25	−25
PDA25@CeO_2	3	2.3	−14	−22
PDA10@CeO_2	3	2.7	−12	−8
PDA10@CeO_2	6	5.4	−6	−1

The conductivity of the aged membranes was also determined at 80 °C and 90% RH (Table 2). The percentage decrease in conductivity with respect to the initial membrane conductivity reflects qualitatively the trend of the weight changes. Thus, both the weight and conductivity of the aged membranes are consistent with the FER data.

Based on the results of ex situ characterization, the membrane loaded with 6 wt% PDA10@CeO_2 (hereafter AQ-PDA@CeO_2) was selected for MEA realization and in situ characterized by OCV stress tests. Hydrogen crossover measurements were carried out

before and during the stress tests after 24 and 47 h from the beginning to check the stability of the membrane. Figure 11 shows the OCV vs. time curves for the bare Aquivion membrane (AQ) and a composite membrane containing 5 wt% CeO_2 (AQ-CeO_2). In all cases, after a non-linear drop during the first 3 h, the cell potential decays linearly as a function of time. The same trend is also observed in the time interval between hours 24 and 47 for AQ-PDA@CeO_2 and AQ after the second hydrogen crossover determination (AQ-CeO_2 stopped working).
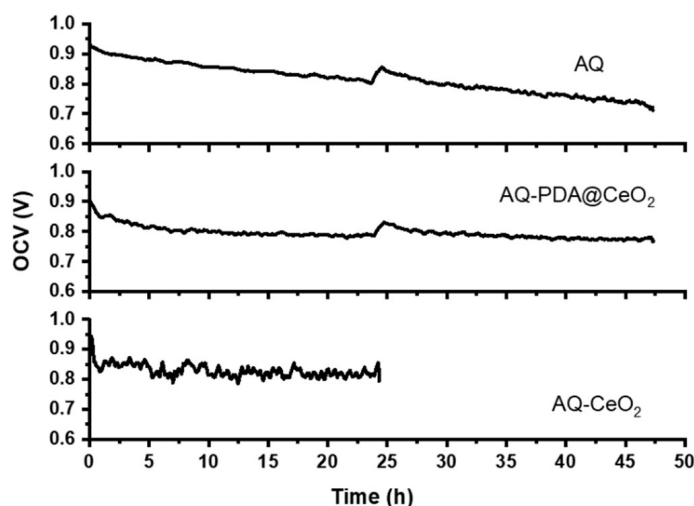

Figure 11. OCV vs. time curves for AQ, AQ-PDA@CeO_2 and AQ-CeO_2 membranes.

The OCV decay rate in the linear regions (Table 3) is lower for AQ-PDA@CeO_2 than for AQ both in the first and in the second time interval of the stress test; as a consequence, the overall OCV decay is ~15% for AQ-PDA@CeO_2 and ~25% for AQ. Moreover, during the first interval, the decay rate of AQ-PDA@CeO_2 and AQ@CeO_2 is similar, thus confirming that the PDA coating does not compromise the radical scavenger activity of CeO_2.

Table 3. OCV decay rate for the indicated membranes at 80 °C and 50% RH.

Membrane	OCV Decay Rate (mV h^{-1})		Overall OCV Percentage Loss
	Hour 4–24	**Hour 28–47**	
AQ-PDA@CeO_2	1.6	1.5	14.7
AQ-CeO_2	1.6		15.8
AQ	4.0	4.2	24.6

Consistently with the evolution of the OCV decay rate, the increase in the hydrogen crossover during the stress test (Table 4) is much larger for AQ (~23 times) than for AQ-PDA@CeO_2 (~2 times).

Table 4. Hydrogen crossover for the indicated membranes at 80 °C and 50% RH.

Membrane	H$_2$ Crossover at 400 mV (mA cm^{-2})		
	Beginning	**24 h**	**47 h**
AQ-PDA@CeO_2	5.5	12	129
AQ-CeO_2	1.4	2.3	
AQ	3.4	5.4	6.6

4. Conclusions

Polymerization of dopamine in water suspensions of CeO_2 allowed preparation of three types of PDA coated CeO_2 nanoparticles containing 10, 25 and 50 wt% PDA. These

materials were used as fillers of Aquivion membranes to improve their chemical stability towards hydroxyl and hydroperoxyl radicals while hindering as much as possible the reaction between the oxide surface and the sulfonic groups of the ionomer.

Composite membranes, loaded with 3 and 5 wt% of each filler, were characterized by conductivity measurements and accelerated degradation tests (based on the Fenton reaction) to assess the radical scavenger efficiency of the filler, and the results of these investigations were compared with those obtained, under the same conditions, for Aquivion membranes containing bare CeO_2 or Bz@ CeO_2. It was found that the decrease in conductivity associated with the increase in the CeO_2 loading is appreciably less severe for membranes containing PDAx@CeO_2 than for those containing bare CeO_2, especially at 110 °C and 50% RH. Moreover, the FER of membranes filled with PDAx@CeO_2 is significantly lower than that of membranes containing Bz@CeO_2 and, for CeO_2 percentage up to 4 wt%, it is coincident with that of membranes loaded with bare CeO_2. Therefore, the PDA coating prevents to a large extent the decrease in conductivity without compromising the radical scavenger activity of CeO_2. Interestingly, the radical scavenger efficiency of PDAx@CeO_2 is nearly unaffected by the PDA content as also proved by the results of the OCV stress tests.

References

1. Wu, J.; Yuan, X.Z.; Martin, J.J.; Wang, H.; Zhang, J.; Shen, J.; Wu, S.; Merida, W. A review of PEM fuel cell durability: Degradation mechanisms and mitigation strategies. *J. Power Sources* **2008**, *184*, 104–119. [CrossRef]
2. Luo, X.; Ghassemzadeh, L.; Holdcroft, S. Effect of free radical-induced degradation on water permeation through PFSA ionomer membranes. *Int. J. Hydrog. Energy* **2015**, *40*, 16714–16723. [CrossRef]
3. Danilczuk, M.; Coms, F.D.; Schlick, S. Visualizing chemical reactions and crossover processes in a fuel cell inserted in the ESR resonator: Detection by spin trapping of oxygen radicals, nafion-derived fragments, and hydrogen and deuterium atoms. *J. Phys. Chem. B* **2009**, *113*, 8031–8042. [CrossRef] [PubMed]
4. Danilczuk, M.; Coms, F.D.; Schlick, S. Fragmentation of fluorinated model compounds exposed to oxygen radicals: Spin trapping ESR experiments and implications for the behaviour of proton exchange membranes used in fuel cells. *Fuel Cells* **2008**, *8*, 436–452. [CrossRef]
5. Zatoń, M.; Rozière, J.; Jones, D.J. Current understanding of chemical degradation mechanisms of perfluorosulfonic acid membranes and their mitigation strategies: A review. *Sustain. Energ. Fuels* **2017**, *1*, 409–438. [CrossRef]
6. Collier, A.; Wang, H.; Zi, Y.X.; Zhang, J.; Wilkinson, D.P. Degradation of polymer electrolyte membranes. *Int. J. Hydrog. Energy* **2006**, *31*, 1838–1854. [CrossRef]
7. Zatoń, M.; Rozière, J.; Jones, D.J. Mitigation of PFSA membrane chemical degradation using composite cerium oxide–PFSA nanofibers. *J. Mater. Chem.* **2017**, *A5*, 5390–5401. [CrossRef]
8. Coms, F.D.; Liu, H.; Owejan, J.E. Mitigation of perfluorosulfonic acid membrane chemical degradation using cerium and manganese Ions. *ECS Trans.* **2008**, *16*, 1735–1747. [CrossRef]
9. Trogadas, P.; Parrondo, J.; Ramani, V. Degradation mitigation in polymer electrolyte membranes using cerium oxide as a regenerative free-radical scavenger. *Electrochem. Solid-State Lett.* **2008**, *11*, B113–B116. [CrossRef]
10. Wang, L.; Advani, S.G.; Prasad, A.K. Degradation reduction of polymer electrolyte membranes using CeO_2 as a free-radical scavenger in catalyst layer. *Electrochim. Acta* **2013**, *109*, 775–780. [CrossRef]

11. Lei, M.; Yang, T.Z.; Wang, W.J.; Huang, K.; Zhang, Y.C.; Zhang, R.; Jiao, R.Z.; Fu, X.L.; Yang, H.J.; Wang, Y.G.; et al. One-dimensional manganese oxide nanostructures as radical scavenger to improve membrane electrolyte assembly durability of proton exchange membrane fuel cells. *J. Power Sources* **2013**, *230*, 96–100. [CrossRef]

12. D'Urso, C.; Oldani, C.; Baglio, V.; Merlo, L.; Aricò, A.S. Fuel cell performance and durability investigation of bimetallic radical scavengers in Aquivion® perfluorosulfonic acid membranes. *Int. J. Hydrog. Energy* **2017**, *42*, 27987–27994. [CrossRef]

13. Wong, C.Y.; Wong, W.Y.; Ramya, K.; Khalid, M.; Loh, K.S.; Daud, W.R.W.; Lim, K.L.; Walvekar, R.; Kadhum, A.A.H. Additives in proton exchange membranes for low- and high-temperature fuel cell applications: A review. *Int. J. Hydrog. Energy* **2019**, *12*, 6116–6135. [CrossRef]

14. Saccà, A.; Gatto, I.; Carbone, A.; Pedicini, R.; Maisano, S.; Stassi, A.; Passalacqua, E. Influence of doping level in Yttria-Stabilised-Zirconia (YSZ) based-fillers as degradation inhibitors for proton exchange membranes fuel cells (PEMFCs) in drastic conditions. *Int. J. Hydrog. Energy* **2019**, *44*, 31445–31457. [CrossRef]

15. Xing, Y.; Li, H.; Avgouropoulos, G. Research progress of proton exchange membrane failure and mitigation strategies. *Materials* **2021**, *14*, 2591. [CrossRef] [PubMed]

16. Donnadio, A.; D'Amato, R.; Marmottini, F.; Panzetta, G.; Pica, M.; Battocchio, C.; Capitani, D.; Ziarelli, F.; Casciola, M. On the evolution of proton conductivity of Aquivion membranes loaded with CeO$_2$ based nanofillers: Effect of temperature and relative humidity. *J. Membr. Sci.* **2019**, *574*, 17–23. [CrossRef]

17. Ball, V. Polydopamine nanomaterials: Recent advances in synthesis methods and applications. *Front. Bioeng. Biotechnol.* **2018**, *6*, 109–121. [CrossRef] [PubMed]

18. Dreyer, D.R.; Miller, D.J.; Freeman, B.D.; Paul, D.R.; Bielawski, C.W. Perspectives on poly(dopamine). *Chem. Sci.* **2013**, *4*, 3796–3802. [CrossRef]

19. Sedó, J.; Saiz-Poseu, J.; Busqué, F.; Ruiz-Molina, D. Catechol-based biomimetic functional materials. *Adv. Mater.* **2013**, *25*, 653–701. [CrossRef]

20. D'Ischia, M.; Napolitano, A.; Ball, V.; Chen, C.T.; Buehler., M.J. Polydopamine and eumelanin: From structure-property relationships to a unified tailoring strategy. *Acc. Chem. Res.* **2014**, *47*, 3541–3550. [CrossRef]

21. Ryu, J.H.; Messersmith, P.B.; Lee, H. Polydopamine surface chemistry: A decade of discovery. *ACS Appl. Mater. Interfaces* **2018**, *10*, 7523–7540. [CrossRef]

22. Liebscher, J.; Mrówczyński, R.; Scheidt, H.A.; Filip., C.; Hădade, N.D.; Turcu, R.; Bende, A.; Beck, S. Structure of polydopamine: A never-ending story? *Langmuir* **2013**, *29*, 10539–10548. [CrossRef]

23. Ding, Y.; Weng, L.T.; Yang, M.; Yang, Z.; Lu, X.; Huang, N.; Leng, Y. Insights into the aggregation/deposition and structure of a polydopamine film. *Langmuir* **2014**, *30*, 12258–12269. [CrossRef] [PubMed]

24. Alfieri, M.L.; Panzella, L.; Oscurato, S.L.; Salvatore, M.; Avolio, R.; Errico, M.E.; Maddalena, P.; Napolitano, A.; d'Ischia, M. The chemistry of polydopamine film formation: The amine-quinone interplay. *Biomimetics* **2018**, *3*, 26. [CrossRef] [PubMed]

25. Tamakloe, W.; AdjeiAgyeman, D.; Park, M.; Yang, J.; Kang, Y.M. Polydopamine-induced surface functionalization of carbon nanofibers for Pd deposition enabling enhanced catalytic activity for the oxygen reduction and evolution reactions. *J. Mater. Chem. A* **2019**, *7*, 7396–7405. [CrossRef]

26. Oh, K.H.; Choo, M.J.; Lee, H.; Park, K.H.; Park, J.K.; Choi, J.W. Mussel-inspired polydopamine-treated composite electrolytes for long-term operations of polymer electrolyte membrane fuel cells. *J. Mater. Chem. A* **2013**, *1*, 14484–14490. [CrossRef]

27. Lee, H.; Dellatore, S.M.; Miller, W.M.; Messersmith, P.B. Mussel-inspired surface chemistry for multifunctional coatings. *Science* **2007**, *318*, 426–430. [CrossRef]

28. Hong, S.; Lee, J.S.; Ryu, J.; Lee, S.H.; Lee, D.Y.; Kim, D.P.; Park, C.B.; Lee, H. Bio-inspired strategy for on-surface synthesis of silver nanoparticles for metal/organic hybrid nanomaterials and LDI-MS substrates. *Nanotechnology* **2011**, *22*, 494020–494027. [CrossRef]

29. Lee, H.; Lee, Y.H.; Statz, A.R.; Rho, J.; Park, T.G.; Messersmith, P.B. Substrate-independent layer-by-layer assembly by using mussel-adhesive-inspired polymers. *Adv. Mater.* **2008**, *20*, 1619–1623. [CrossRef]

30. Ho, C.C.; Ding, S.J. Structure, properties and applications of mussel-inspired polydopamine. *J. Biomed. Nanotechnol.* **2014**, *10*, 3063–3084. [CrossRef]

31. Kang, S.M.; Hwang, N.S.; Yeom, J.; Park, S.Y.; Messersmith, P.B.; Choi, I.S.; Langer, R.; Anderson, D.G.; Lee, H. One-step multipurpose surface functionalization by adhesive catecholamine. *Adv. Funct. Mater.* **2012**, *22*, 2949–2955. [CrossRef]

32. Lynge, M.E.; van der Westen, R.; Postma, A.; Stadler, B. Polydopamine—A nature-inspired polymer coating for biomedical science. *Nanoscale* **2011**, *3*, 4916–4928. [CrossRef]

33. Ju, K.Y.; Lee, Y.; Lee, S.; Park, S.B.; Lee, J.K. Bioinspired polymerization of dopamine to generate melanin-like nanoparticles having an excellent free-radical-scavenging property. *Biomacromolecules* **2011**, *12*, 625–632. [CrossRef] [PubMed]

34. Liu, Y.; Ai, K.; Lu, L. Polydopamine and its derivative materials: Synthesis and promising applications in energy, environmental, and biomedical fields. *Chem. Rev.* **2014**, *114*, 5057–5115. [CrossRef] [PubMed]

35. Martín, M.; Salazar, P.; Villalonga, R.; Campuzano, S.; Pingarrond, J.M.; González-Mora, J.L. Preparation of core–shell Fe$_3$O$_4$@poly(dopamine) magnetic nanoparticles for biosensor construction. *J. Mater. Chem. B* **2014**, *2*, 739–746. [CrossRef]

36. Fedorenko, V.; Damberga, D.; Grundsteins, K.; Ramanavicius, A.; Ramanavicius, S.; Emerson Coy, E.; Iatsunskyi, I.; Viter, R. Application of polydopamine functionalized zinc oxide for glucose biosensor design. *Polymers* **2021**, *13*, 2918. [CrossRef] [PubMed]

37. Black, K.C.; Yi, J.; Rivera, J.G.; Zelasko-Leon, D.C.; Messersmith, P.B. Polydopamine-enabled surface functionalization of gold nanorods for cancer cell-targeted imaging and photothermal therapy. *Nanomedicine* **2013**, *8*, 17–28. [CrossRef]

38. Liu, T.; Kim, K.C.; Lee, B.; Chen, Z.; Noda, S.; Jang, S.S.; Lee, S.W. Self-polymerized dopamine as an organic cathode for Li- and Na-Ion batteries. *Energy Environ. Sci.* **2017**, *10*, 205–215. [CrossRef]

39. He, Y.; Wang, J.; Zhang, H.; Zhang, T.; Zhang, B.; Cao, S.; Liu, J. Polydopamine-modified graphene oxide nanocomposite membrane for proton exchange membrane fuel cell under anhydrous conditions. *J. Mater. Chem. A* **2014**, *2*, 9548–9558. [CrossRef]

40. Wang, J.; Bai, H.; Zhang, H.; Zhao, L.; Chen, H.; Li, Y. Anhydrous proton exchange membrane of sulfonated poly(ether ether ketone) enabled by polydopamine-modified silica nanoparticles. *Electrochim. Acta* **2015**, *152*, 443–455. [CrossRef]

41. Wang, J.; Gong, C.; Wen, S.; Liu, H.; Qin, C.; Xiong, C.; Dong, L. A facile approach of fabricating proton exchange membranes by incorporating polydopamine-functionalized carbon nanotubes into chitosan. *Int. J. Hydrog. Energy* **2019**, *44*, 6909–6918. [CrossRef]

42. Zhang, H.; Zhang, T.; Wang, J.; Pei, F.; He, Y.; Liu, J. Enhanced proton conductivity of sulfonated poly(ether ether ketone) membrane embedded by dopamine-modified nanotubes for proton exchange membrane fuel cell. *Fuel Cells* **2013**, *13*, 1155–1165. [CrossRef]

43. Zhou, J.; Duan, B.; Fang, Z.; Song, J.; Wang, C.; Messersmith, P.B.; Duan, H. Interfacial assembly of mussel-inspired Au@Ag@ polydopamine core-shell nanoparticles for recyclable nanocatalysts. *Adv. Mater.* **2014**, *26*, 701–705. [CrossRef] [PubMed]

44. Yoon, K.R.; Lee, K.A.; Jo, S.; Yook, S.H.; Lee, K.Y.; Kim, L.D.; Kim, J.Y. Mussel-inspired polydopamine-treated reinforced composite membranes with self-supported CeOx radical scavengers for highly stable PEM fuel cells. *Adv. Funct. Mater.* **2019**, *29*, 1806929. [CrossRef]

45. Casciola, M.; Donnadio, A.; Sassi, P. A critical investigation of the effect of hygrothermal cycling on hydration and in-plane/through-plane proton conductivity of Nafion 117 at medium temperature (70–130 °C). *J. Power Sour.* **2013**, *235*, 129–134. [CrossRef]

46. Capitani, D.; Casciola, M.; Donnadio, A.; Vivani, R. High yield precipitation of crystalline α-zirconium phosphate from oxalic acid solutions. *Inorg. Chem.* **2010**, *49*, 9409–9415. [CrossRef]

47. Gatto, I.; Saccà, A.; Baglio, V.; Aricò, A.S.; Oldani, C.; Merlo, L.; Carbone, A. Evaluation of hot-pressing parameters on the electrochemical performance of MEAs based on Aquivion® PFSA membranes. *J. Energy Chem.* **2019**, *35*, 168–173. [CrossRef]

48. Gatto, I.; Carbone, A.; Saccà, A.; Passalacqua, E.; Oldani, C.; Merlo, L.; Sebastiána, D.; Aricò, A.S.; Baglio, V. Increasing the stability of membrane-electrode assemblies based on Aquivion® membranes under automotive fuel cell conditions by using proper catalysts and ionomers. *J. Electroanal. Chem.* **2019**, *842*, 59–65. [CrossRef]

49. Luo, H.; Gu, C.; Zheng, W.; Dai, F.; Wang, X.; Zheng, Z. Facile synthesis of novel size-controlled antibacterial hybrid spheres using silver nanoparticles loaded with poly-dopamine spheres. *RSC Adv.* **2015**, *5*, 13470–13477. [CrossRef]

50. Silverstein, R.; Bassler, G.; Morrill, R. *Spectrometric Identification of Organic Compounds*; John Wiley & Sons: New York, NY, USA, 1981.

51. Zangmeister, R.A.; Morris, T.A.; Tarlov, M.J. Characterization of polydopamine thin films deposited at short times by autoxidation of dopamine. *Langmuir* **2013**, *29*, 8619–8628. [CrossRef]

52. Knorr, D.B., Jr.; Tran, N.T.; Gaskell, K.J.; Orlicki, J.A.; Woicik, J.C.; Fischer, D.A.; Lenhart, J.L. Synthesis and characterization of aminopropyltriethoxysilane-polydopamine coatings. *Langmuir* **2016**, *32*, 4370–4381. [CrossRef] [PubMed]

53. Stöhr, J. *NEXAFS Spectroscopy*; Springer-Verlag: Berlin/Heidelberg, Germany, 1992.

54. Feyer, V.; Plekan, O.; Richter, R.; Coreno, M.; Prince, K.C.; Carravetta, V. Photoemission and photo absorption spectroscopy of glycyl-glycine in the gas phase. *J. Phys. Chem. A* **2009**, *113*, 10726–10733. [CrossRef] [PubMed]

55. Stewart-Ornstein, J.; Hitchcock, A.P.; Hernández Cruz, D.; Henklein, P.; Overhage, J.; Hilpert, K.; Hale, J.D.; Hancock, R.E. Using intrinsic X-ray absorption spectral differences to identify and map peptides and proteins. *J. Phys. Chem. B* **2007**, *111*, 7691–7699. [CrossRef] [PubMed]